Materials Research. 2022; 25:e20210164
DOI: https://doi.org/10.1590/1980-5373-MR-2021-0164

Magnetic Particles Nanorod of ZnO/$CuFe_2O_4$ Prepared by Green Synthesized Approach: Structural, Optical and Magnetic Properties, and Photocatalytic Activity

***Rahmayeni*[a]*, *Nurul Azizah*[a], *Yeni Stiadi*[a], *Yulia Eka Putri*[a], *Zulhadjri*[a]**

[a]*Andalas University, Faculty of Mathematics and Natural Sciences, Department of Chemistry, Kampus Limau Manis, Padang, 25163, Indonesia*

Received: April 5, 2021; Revised: September 9, 2021; Accepted: November 12, 2021.

In this study, magnetically separable ZnO/$CuFe_2O_4$ nanorod particles were synthesized by the green synthesis approach, using rambutan peel extract (*Nephelium lappaceum* L.) as a capping agent. The samples were evaluated as photocatalyst for the degradation of Rhodamine B dye driven by solar light irradiation. The XRD patterns represented the specific peaks of ZnO and $CuFe_2O_4$ in the ZnO/$CuFe_2O_4$ composite. SEM and TEM images showed the rod-like shape of the ZnO/$CuFe_2O_4$ composite synthesized using 3 mL (ZCuE3N) of rambutan peel extract. ZCuE3N sample has an increase in photocatalytic activity up to 98.8% in the degradation of Rhodamine B under solar light irradiation for 2 h. Magnetic measurement by VSM revealed that ZnO/$CuFe_2O_4$ composite was superparamagnetic. ZnO/$CuFe_2O_4$ composites remained stable in an air atmosphere and exhibited promise as a reusable photocatalyst as it can be easily separated from the solution by an external magnetic field.

Keywords: *ZnO/$CuFe_2O_4$ nanorod, green synthesis, Nephelium lappaceum L, Rhodamine B.*

1. Introduction

Access to clean water is an important and valuable necessity in life. However, the presence of pollutants in water is a significant barrier to assessing clean water. Dyes have been identified as the most prominent chemical contaminants in water pollution and cannot be naturally degraded by microbes. Various dyes are commonly used in the textile industry, such as Rhodamine B, Direct Red, Direct Yellow, and Methylene Blue. These dyes generally contain azo groups (N = N), known to be toxic and carcinogenic in the human body. Moreover, they have high pigmentation and are extremely hazardous to flora, fauna, and humans at their low concentration level. Several methods have been applied to remove dyes from the environment, including sedimentation, adsorption, chemical precipitation, and biological processes. However, these methods create new waste problems due to fractional degradation of organic dyes and the production of a large volume of toxic sludge[1–4]. Thus, to achieve complete degradation of dyes from wastewater, a more effective treatment method is needed. The photocatalytic process uses semiconductor materials such as TiO_2, WO_3, Bi_2O_3, ZnO, Fe_2O_3, CdS, CdO, and ZnS as heterogeneous photocatalysts is a promising solution to solve this problem[5,6].

Among various heterogeneous photocatalysts, ZnO has received significant attention due to its attractive properties such as electric, photonic, oxidation resistance, non-toxic, rapid electron transfer, and wide bandgap[7]. In particular, ZnO is an n-type semiconductor, has received special attention because of its good photocatalytic activity. Besides, ZnO material has some advantages of being environmentally friendly, chemically stable, easy to prepare, morphologically controlled, and high photosensitivity. In addition, as a photocatalyst, ZnO has a wide bandgap range (3 - 4 eV), which enables it to effectively absorb in UV light region and less in visible light[8]. ZnO's combination with ferrites demonstrated a synergistic effect to enhance the photocatalytic activity under UV and visible-light irradiations[9].

Spinel ferrite MFe_2O_4 (M = Co, Ni, Cu, Zn, etc.) is a p-type semiconductor with magnetic behaviors. It has attracted the attention of researchers due to its potential in several applications [10]. Within this group of compounds, copper ferrite ($CuFe_2O_4$) is of particular interest because of its attractive properties such as recyclability, magnetic and chemical properties, and structural stability, as well as a wider absorption area[11]. However, pure $CuFe_2O_4$ showed a poor catalytic performance owing to its low electron transfer rate, which limits its application as a heterogeneous catalyst[12]. Thus, the formation of ZnO/$CuFe_2O_4$ composites gives advantages of improved photocatalytic and magnetic properties, chemical stability, and easier recyclability. This combination will reduce the energy gap of ZnO so that it works well in the visible (sun) region as well as brings out the magnetic properties of catalyst to be separated using an external magnet.

Several researchers have investigated the synthesis of ZnO/$CuFe_2O_4$ composites. Ali et al. reported the synthesis of ZnO/$CuFe_2O_4$ by wet chemical preparation resulted in nanodisc shape, the thickness of 20-70 nm, and the appearance of superparamagnetic behavior[13]. Karunakaran et al. prepared nanoplates ZnO/$CuFe_2O_4$ by the hydrothermal method and then identified its superparamagnetic behavior, sustainable photocatalytic activity, and anti-bacterial properties[14]. Kumar et al. also reported ZnO/$CuFe_2O_4$ synthesis supported by the graphene oxide route one-step combustion[15]. The cubic-$CuFe_2O_4$/ZnO nanofibers (c-CFZs) with enhanced visible-light photocatalytic

*email: rahmayenni@sci.unand.ac.id

activity and magnetic separation were synthesized by the electrospinning technique combined with the coprecipitation method[11]. Sara Paydar et al. had synthesized the faceted and regular shape of ZnO/$CuFe_2O_4$ by the glycine-nitrate process followed by photo-deposition[16]. However, there are no reports about the synthesis of rod-like ZnO/$CuFe_2O_4$ through a green synthesis approach using rambutan peel extract as a capping agent and stabilizer with the application as a photocatalyst for Rhodamine B dye degradation under solar light.

Rambutan (*Nephelium lappaceum* L.) is a type of sub-tropical fruit and its residues consist principally of seeds and peels waste[17]. In Indonesia, rambutan is a plant that is widely cultivated for its fruit. Rambutan peel contains secondary metabolite compounds such as polyphenols, where the aromatic hydroxyl group in polyphenolic acid has functions as a capping agent that regulates the formation of material structures to be more regular and homogeneous. The phenolic hydroxyl groups of polyphenols from the p-track conjugation effect when the hydroxyl groups form binding with the metal as metal phenolate complex (metal-ellagate complex) by the chelating effect. The obtained metal-ellagate complex on heat treatment yields metal oxide nanocrystals[17–19]. Rahmayeni et al. had used rambutan peel extract to synthesis ZnO/$CoFe_2O_4$ composites[20]. Currently, the use of natural extracts as a substitute for environmentally harmful chemicals in the synthesis of materials has become the preferred solution[21,22].

This paper reports nanorod ZnO/$CuFe_2O_4$ composite synthesis by the green chemistry approach using the hydrothermal method in the presence of rambutan peel extract as a capping agent. The as-synthesized samples characterized using several devices show the rod-like shape, superparamagnetic properties, and adsorption in the visible light area. The photocatalytic activity carried out involved the degradation of Rhodamine B as one of the toxic dye under direct solar light irradiation. It revealed that this material could be used as a catalyst to treat organic pollutants in wastewater. Several parameters related to the photocatalytic process were also investigated in this work.

2. Experimental

2.1. Material

All materials used in this study were of analytical grade without further purification. The materials used in this work were [$Zn(NO_3)_2.6H_2O$] (Merck), [$Cu(NO_3)_2.3H_2O$] (Merck), [$Fe(NO_3)_3.9H_2O$] (Merck), ethanol (Merck), NaOH (Merck), and Rhodamine B dye. Rambutan fruit (*Nephelium lappaceum* L.) peels were obtained from Limau Manis in Padang City, West Sumatra. All solutions were prepared using deionized water.

2.2. Preparation of rambutan fruit peel extract

The rambutan peels were cut into small pieces, washed with water, and dried at 50°C. After that, the dried rambutan peels were finely ground into powder. Three g of rambutan peel powder was dissolved in 60 mL ethanol solution (40 mL distilled water and 20 mL ethanol). Then, the mixture was stirred at 80°C for 10 minutes at a speed of 500 rpm. The rambutan peel extract was separated from the pulp and stored in the refrigerator for further use.

2.3. Synthesis of $CuFe_2O_4$ particles

Synthesis of $CuFe_2O_4$ material using rambutan peel extract was carried out by the hydrothermal method[23]. A total of 1:2 molar ratio of Cu^{2+}:Fe^{3+} was mixed in 40 mL solution of distilled water and rambutan peel extract (variations of rambutan peel extracts of 1, 3, 5, and 7 mL) to determine the effects of extract volume on the nature of the synthesized material. The mixtures were stirred at a speed of 500 rpm for 3 h, and the pH was adjusted to 12 by the addition of 2 M NaOH. The mixtures were poured into an autoclave and heated at 180°C for 3 h. The precipitate was filtered and washed with distilled water to remove the organic compound of extract and attain a neutral pH. The product then dried at 110°C for 3 h. The final products were denoted as CuE1N, CuE3N, CuE5N, and CuE7N for rambutan peel extracts of 1, 3, 5, and 7 mL, respectively.

2.4. Synthesis of ZnO/$CuFe_2O_4$ nanocomposites

Synthesis of ZnO/$CuFe_2O_4$ nanocomposites was also carried out by the hydrothermal method. The synthesis of composite particles was done by adopted the previous procedures[24,25]. $Zn(NO_3)_2.4H_2O$ and $CuFe_2O_4$ (from procedure 2.3) with a molar ratio of Zn^{2+}: $CuFe_2O_4$ of 1: 0.05 were added to 40 mL solution containing the distilled water and extract solution. Then, the mixtures were stirred at a speed of 500 rpm for 3 h, and the pH was adjusted to 12 by slowly adding 2 M NaOH. After that, the mixture was poured into an autoclave and heated at 180°C for 3 h. The precipitate was filtered and washed with distilled water to a neutral pH and then dried at 110°C for 3 h. The composite products were denoted as ZCuE1N, ZCuE3N, ZCuE5N, and ZCuE7N for the volume variation of rambutan peel extract of 1, 3, 5, and 7 mL in $CuFe_2O_4$, respectively.

2.5. Characterization of the samples

The phase formation of prepared samples was analyzed by X-ray diffractometer (PANalytical X'pert Pro Multipurpose Diffractometer with Cu-Kα radiation). FT-IR spectra were recorded using a Nicolet IR200 FT-IR spectrometer by utilizing the KBr pellet technique. The surface morphology and chemical composition of samples were examined by field-emission scanning electron microscope (FESEM, JEOL JSM-6360LA) embedded with energy-dispersive X-ray spectroscopy (EDS). Next, the detailed morphology of the samples was investigated using a transmission electron microscope (TEM, JEM-1400). High-resolution transmission electron microscopy (HRTEM; FEI Technai G2, F30) was employed to probe the microstructure, particle size distribution, and high-resolution imaging of the sample. The absorption measurement of samples was analyzed by UV–Vis spectrophotometer (Shimadzu UV-Vis 2450). The magnetic properties of the samples were investigated using a vibrating sample magnetometer (VSM OXFORD 1.2H).

2.6. Photocatalytic activity

The photocatalytic activities of all samples were evaluated by the degradation of Rhodamine B dye under

solar light irradiation. This procedure was adopted from previous research studies[20]. In a typical process, 20 mg of CuE5N, ZnO, ZCuE3N, ZCuE5N, and ZCuE7N catalysts were suspended in 20 mL aqueous solution of Rhodamine B (10 mg L^{-1}). Before exposure under solar light, the suspension was stirred in the dark to ensure the solution's adsorption/desorption on catalysts. Consequently, the suspension was irradiated under direct solar light for 2 h (from 11:00 am to 1:00 pm) outdoor. After that, distilled water was added to the suspension to equalize the volume to the initial volume after evaporation during the irradiation process. Then, the supernatant was separated from the catalyst using external magnetic, and the absorption of the solution was measured by the UV-vis spectrophotometer at a wavelength of 553 nm to evaluate the photodegradation process. Several parameters related to the photocatalytic activity test were also investigated, including the concentration of dye, irradiation time, and type of catalyst.

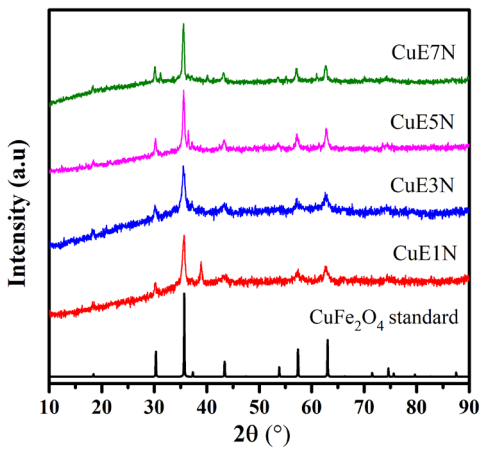

Figure 1. XRD patterns CuE1N, CuE3N, CuE5N, and CuE7N.

3. Results and Discussion

3.1. Characterization

XRD analysis was carried out to determine the crystal structure and size of the synthesized samples. Figure 1 shows the XRD patterns of $CuFe_2O_4$ products synthesized hydrothermally using rambutan peel extracts with different concentrations. From the shape of the XRD patterns, it can be seen that the addition of the extract affected the formation of the $CuFe_2O_4$ structure. The variation in the extract concentration in the synthesis of ferrites (1, 3, 5, and 7 mL) for CuE1N, CuE3N, CuE5N, and CuE7N resulted in sharp XRD patterns. Specific peaks of $CuFe_2O_4$ appeared at 2θ = 30.1, 35.6, 43.3, 57.2, 62.8° for hkl 220, 311, 400, 511 and 400, respectively. Based on the XRD pattern, it can be concluded that all samples have spinel cubic structure in accordance with the standard diffraction pattern (ICSD 37429). However, the impurity phase of Fe_2O_3 and CuO were observed in CuE1N, CuE5N, and CuE7N, while for CuE3N no impurities were detected[26]. Therefore, the pure CuE3N sample was used to form the composite samples.

The average crystallite size of $CuFe_2O_4$ calculated using the Scherer equation[25,27] is approximately 7.5 nm, 4.9 nm, 14.8 nm, and 14.7 for samples CuE1N, CuE3N, CuE5N, and CuE7N, respectively. It is suggested that the addition of a small concentration of extract causes the capping agent process to be incomplete, but if the concentration of extract is too large the grain growth process will be disrupted. The as-prepared spinel $CuFe_2O_4$ by the hydrothermal method in the presence of rambutan peel extract is smaller in crystallite size than obtained by[28] using the sol-gel auto combustion method.

The XRD patterns of the ZnO/$CuFe_2O_4$ composites are shown in Figure 2. It can be seen that the specific peaks of ZnO appeared at 2θ = 31.7, 34.4, 36.2, 47.5, 56.5, 62.8, 67.8, and 68.9° with the Miller's index of 110, 002, 101, 102, 110, 103, 200, 112, 201, 004, and 202, respectively[7]. These patterns refer to the hexagonal crystalline structure of

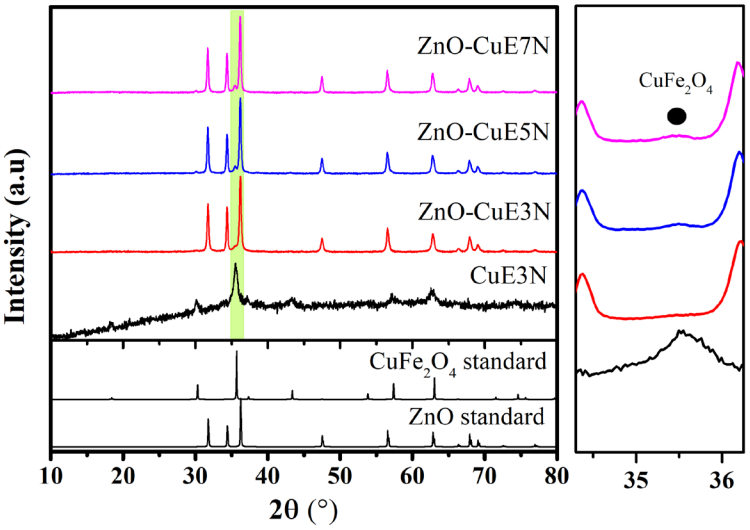

Figure 2. XRD pattern CuE3N and ZCuE3N, ZCuE5N, and ZCuE7N composites.

ZnO which corresponds to ICDD 65121. The specific peak of $CuFe_2O_4$ in the composite was observed at $2\theta = 35.5$ as observed in the enlarged XRD patterns in Figure 2. The intensity of the $CuFe_2O_4$ peak in the XRD pattern is very low due to the relatively small amount of $CuFe_2O_4$ in the composite samples (1:0.05, ZnO:$CuFe_2O_4$). Hence, the diffraction pattern confirms the co-existence of both phases in the nanocomposite sample without an impurity phase. The average crystal size of the composite samples is approximately 32, 40, and 41 nm for ZCuE3N, ZCuE5N, and ZCuE7N, respectively. These average crystal sizes were determined from the average of the three highest XRD peaks from the ZnO phase. These values are smaller than values obtained in previous studies by[13] which prepared the composites without using the plant extracts in their procedure.

Analysis by FT-IR was measured at wavenumbers of 4000-300 cm^{-1} and the characteristic spectrum of $CuFe_2O_4$ spinel ferrite is shown in Figure 3. The presence of two main broad peaks in the range of 450-300 cm^{-1} (ν_1) and 600-500 cm^{-1} (ν_2) observed in the spectrum is associated with the vibration of Cu^{2+}-O^{2-} in the tetrahedral site and Fe^{3+}-O^{2-} in the octahedral site, respectively. Based on the geometrical configuration of the nearest neighbor oxygen, metal ions in ferrite are located in two different sub-lattices, namely tetrahedral (*A*-site) and octahedral (*B*-site)[29]. The vibration peaks at the wavenumber of 1163 cm^{-1}, 1184 cm^{-1}, and 1186 cm^{-1} indicate the presence of Cu-O-Fe vibration in $CuFe_2O_4$ spinel ferrite structure[30]. The result of the FT-IR analysis reinforces the data obtained through XRD analysis.

Figure 4 shows the FT-IR spectrum of ZnO/$CuFe_2O_4$ composites as measured in the range of 4000-300 cm^{-1}. The specific absorption area of Zn-O in ZnO/$CuFe_2O_4$ composite appeared at around 500 cm^{-1} according to the formation of ZnO in composites. This peak at ~500 cm^{-1} also shows the presence of Fe^{3+}-O^{2-} stretching on the tetrahedral site and the ~380 cm^{-1} absorption shows the presence of M^{2+}-O^{2-} (Cu^{2+}, Zn^{2+}) bonds on the octahedral site in composites structure[13].

The morphology of the ZCuE3N, ZCuE5N, and ZCuE7N was analyzed by FESEM as shown in Figure 5. It can be seen that the ZCuE3N composite (Figure 5a) has a homogeneous rod-like grains shape, the ZCuE5N composite (Figure 5b) has granule and rod-like grains shape with slight agglomeration, and the ZCuE7N composite (Figure 5c) formed agglomeration with a mixture of rod-like and cube shapes. FESEM image observation suggested that the use of excess rambutan peel extract resulted in a non-uniform shape and formed agglomeration. We compared our results with the previous work that has been synthesized $CuFe_2O_4$-ZnO composites in the absence of natural extracts and found that the $CuFe_2O_4$-ZnO synthesized with the hydrothermal method has nanoplates particles with larger size[14] and $CuFe_2O_4$-ZnO prepared by the two-step wet chemical coprecipitation method produced grains[13].

The localized elements and their composition in the composite were identified and measured by using EDX spectroscopy. Figure 5d shows the EDX spectrum of the ZCuE3N composite. The EDX analysis of the ZCuE3N composite exhibits the presence of Zn, Fe, Cu, and O. No impurities were observed in this spectrum. The elemental mapping images were further displayed in Figure 6 indicating the distribution of the homogenous elements in CuE3N composite.

To obtain further insight into the ZCuE3N microstructure, this material was analyzed using TEM, HRTEM, and SAED devices (Figure 7). The TEM images of the ZCuE3N composite (Figure 7a-c) revealed a homogeneous nanorod shape with an average particle size of around 200 nm in length and 50 nm in width (aspect ratio is 4), and the image of Figure 7d-e revealed the detailed nanorod particles in ZCuE3N composite. This result revealed that the capping agent from natural extracts has a significant role to control the grain growth process. The synthesized composite particles tend to agglomerate due to their magnetic nature. These nanorod particles are a typical characteristic of ZnO morphology and the black part of the grain is assumed to be $CuFe_2O_4$ ferrite coated by ZnO in the composite. The SAED pattern of the ZCuE3N composite in Figure 7f exhibited the ring pattern of the composite. The combination of crystal structure analysis and morphology observation confirmed that the ZCuE3N composite was polycrystalline with a

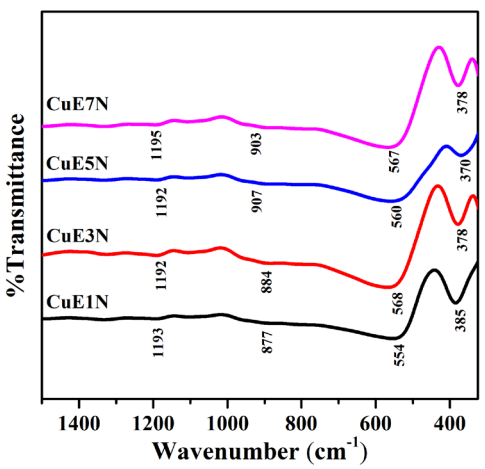

Figure 3. FT-IR spectrum of $CuFe_2O_4$.

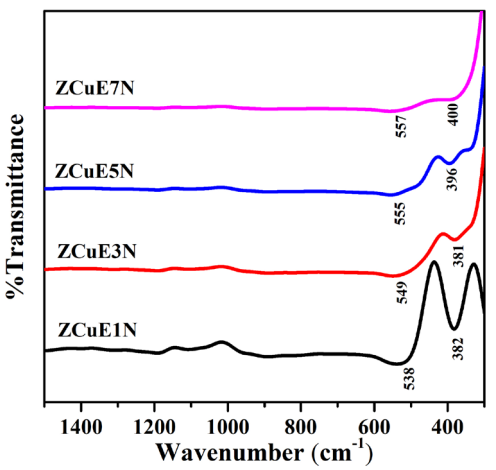

Figure 4. FT-IR spectrum of composites.

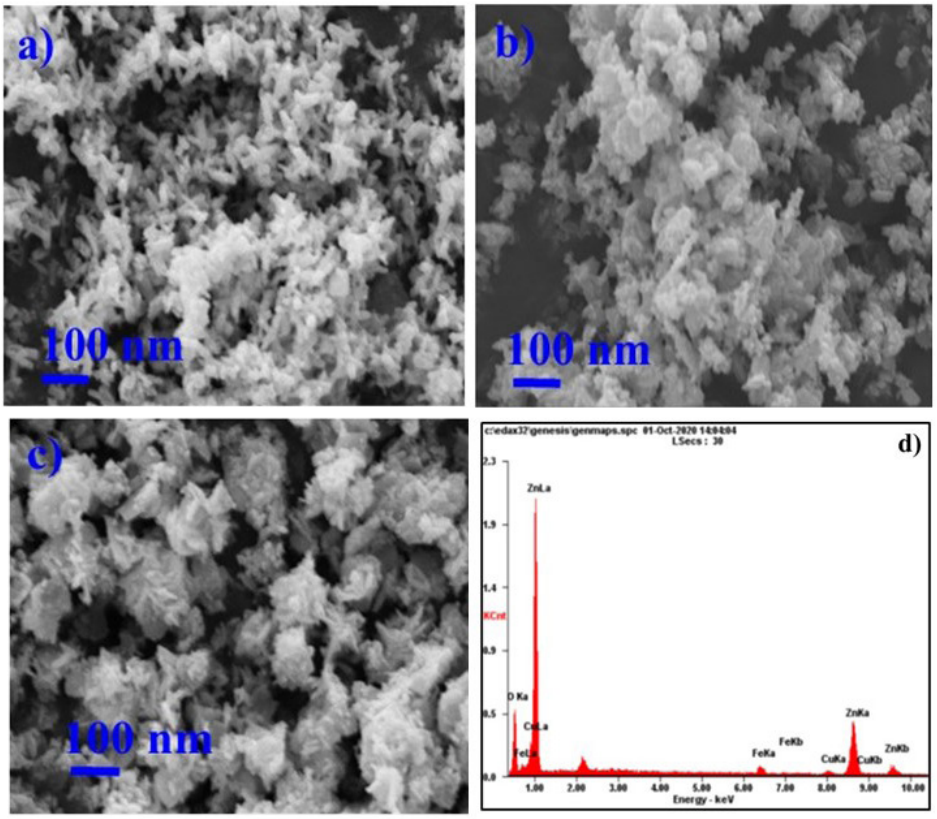

Figure 5. FESEM images of (a) ZCuE3N, (b) ZCuE5N, (c) ZCuE7N, and (d) EDX spectrum of ZCuE3N.

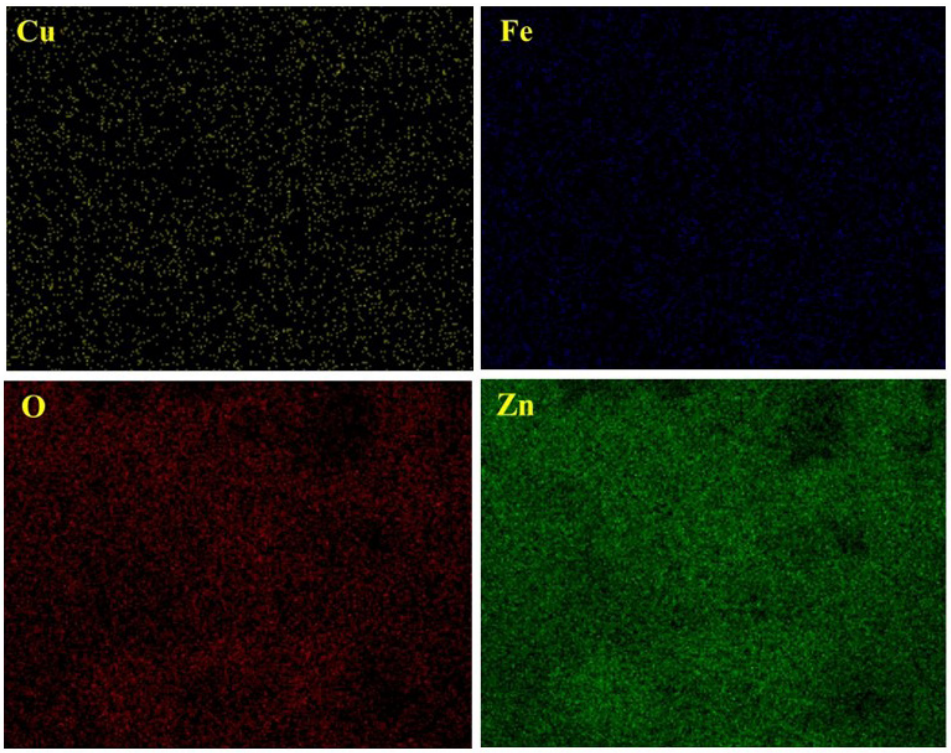

Figure 6. Map of elements distribution of ZCuE3N.

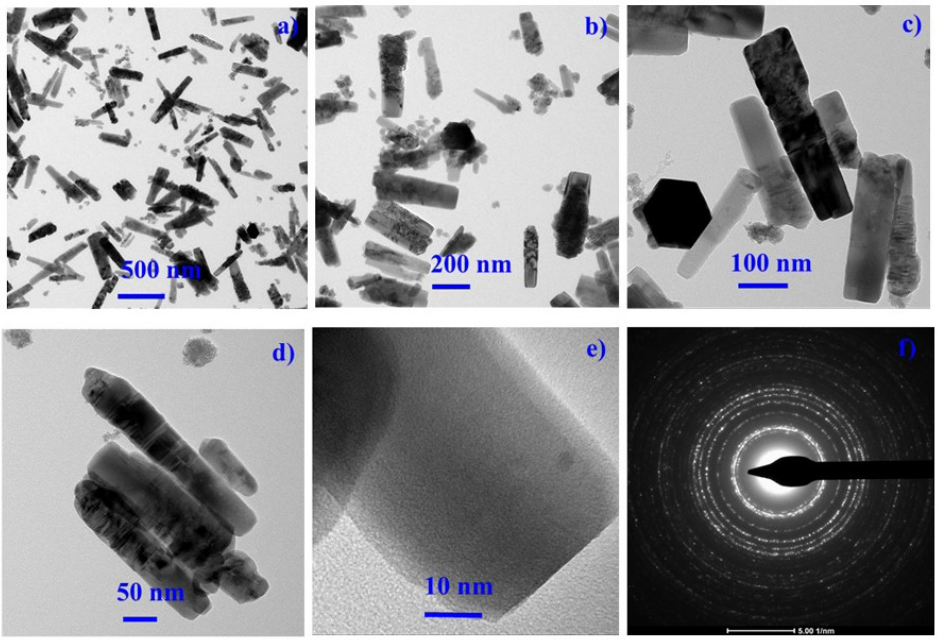

Figure 7. (a-c) TEM images of ZCuE3N nano rod particles at difference magnification, (d-e) HRTM image, and (f) SAED pattern.

high degree of crystallinity and homogenous morphology, containing both $CuFe_2O_4$ and ZnO.

To investigate the optical properties, the samples were analyzed by UV–Vis DRS, and the spectra are shown in Figure 8. The UV-Vis DRS spectrum of CuE3N (Figure 8a) exhibited a high absorption intensity in a broad region from 300 nm to 800 nm. The enhanced absorption in the visible light region of $CuFe_2O_4$ can be attributed to photo-generated electron transition from O 2p orbital into Fe 3d orbital according to the general definition of the energy band structures of $CuFe_2O_4$. The energy bandgap can be estimated using Tauc's relation:

$$(\alpha h\nu)^2 = A\left(h\nu - E_g\right) \quad (1)$$

where, α, hν, A and E_g are optical absorption coefficient, the energy of the incident photon in eV, constant and optical band gap energy in eV[31]. A graph plotted between $[\alpha h\nu]^2$ vs. energy and the optical energy band gap obtained by the extrapolation of the linear area of the plot $[\alpha h\nu]^2 = 0$, is shown in Figure 8a (insert)[32]. The optical energy band gap of $CuFe_2O_4$ was calculated as 2.28 eV. The bandgap value of synthesized $CuFe_2O_4$ was larger than the values obtained by [14,33] which synthesized $CuFe_2O_4$ by the hydrothermal method and solid-state reaction without the use of natural extracts. It is suggested that the use of natural extracts in the synthesis process produces more homogeneous, small, and regular granules, which affect the band gap value.

Figure 8b shows the UV-Vis DRS spectrum of ZCuE3N and ZCuE5N composites with bandgap energies of 2.74 eV and 2.71 eV, respectively. This can be attributed to the formation of a new level between the valence band (VB)

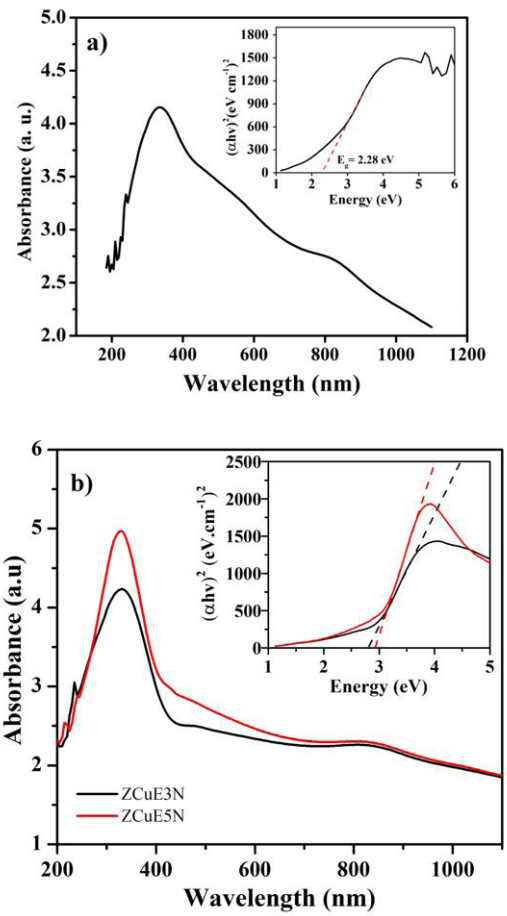

Figure 8. DRS UV-Vis spectrum of (a) CuE3N and (b) composites.

and conduction band (CB) of $CuFe_2O_4$ by coupling with ZnO nanoparticles, which promotes transport mobility and further enhances the absorption. The reduction of the gap in the band energy of ZnO in composites is advantageous for its application as a photocatalyst[17,34]. This bandgap value ensures the suitability of the material as a photocatalyst in visible light or sunlight region.

The effects of extract concentration on the magnetic properties of ferrites and composites were studied by VSM analysis. The magnetic field dependence of the magnetization (*M-H* curve) was performed at room temperature as shown in Figure 9. The curve of $CuFe_2O_4$ (Figure 9a) showed that the *S*-shaped hysteresis loop confirmed the ferrimagnetic behavior with magnetic saturation (M_s) values of 8.71, 11.11, 18.97, and 32.74 emu/g for CuE1N, CuE3N, CuE5N, and CuE7N, respectively. The increase in M_s with increasing the amount of extract concentration is assumed to be due to the formation of bulk particles and the changes of the magnetic structure, affecting the magnetic dipole of material and hence the magnetization. The presence of Fe_2O_3 impurities contributes to the enhancement magnetic properties of $CuFe_2O_4$[35]. Furthermore, the magnetic properties of synthesized CuF_2O_4 samples were lower than the samples obtained from a previous study by[27,36] that prepared the CuF_2O_4 using the combustion method. The reduced magnetic property is advantageous for its application in photocatalytic processes as it reduces agglomeration and is readily separated from liquids.

Moreover, in nanocomposites, the similar hysteresis behavior of ferrites was observed with their M_s values were lower than $CuFe_2O_4$ (Figure 9b). As it is known that ZnO is diamagnetic and $CuFe_2O_4$ is ferrimagnetic, the presence of $CuFe_2O_4$ ferrite raises the magnetic properties of ZnO in the ZCuE3N, ZCuE5N, and ZCuE7N composites to become superparamagnetic with a lower M_s value than $CuFe_2O_4$ (Table 1). The crystallinity of the sample also contributes to the increase in the magnetic properties of ZnO/$CuFe_2O_4$ composites. The magnetic properties possessed by these composites allow them to be withdrawn and separated from the liquid with the help of external magnets, making them very promising as renewable photocatalysts[37,38].

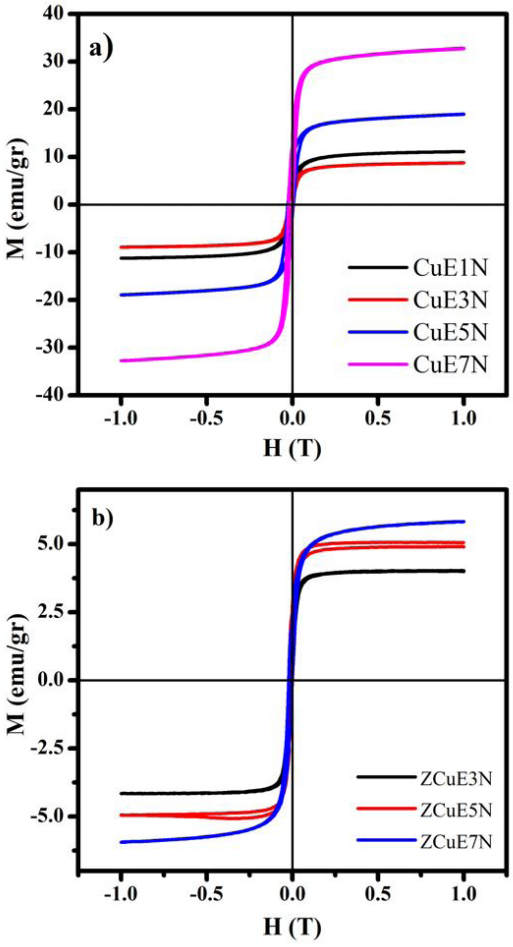

Figure 9. Magnetic hysteresis curve of (a) ferrites and (b) composites.

3.2. Photocatalytic activity of ZnO/$CuFe_2O_4$ composites

The photocatalytic activities of the ZnO, $CuFe_2O_4$, and ZnO/$CuFe_2O_4$ composites were determined by photodegradation of Rhodamine B driven by direct solar light irradiation. The degradation percentage was calculated using the following equation:

$$\%\ degradation = (A_0 - A_t) / A_0 \times 100\% \quad (2)$$

where A_0 and A_t represent the absorbance of Rhodamine B dye solution before and after the solar light irradiation at time *t*, respectively[24,39]. Figure 10 shows the photocatalytic activity of the as-synthesized samples. It is evident from the figure that Rhodamine B was degraded effectively by composites and the highest activity was obtained using ZCuE3N with degradation percentages reaching 98.8% under the solar light irradiation for 2 h. These results are in accordance with TEM analysis findings such as homogeneous morphology, particle distribution, smaller particle size, and no agglomeration in ZCuE3N samples. As a result, these findings are better than those obtained by[11]. Without light, the degradation percentage of ZCuE3N only reaches 4.7% for 2 h. These results prove that the degradation of dye by ZCuE3N occurs through the photocatalytic process since the irradiation process significantly increases the percentage of degradation.

Table 1. The magnetic properties of ferrites and composites (*Ms, Mr, and Hc* values).

Sample	Magnetic saturation (*Ms*)	Magnetic remanent (*Mr*)	Coercive field (*Hc*)
	emu/g		Tesla
CuE1N	8.71	3.63	0.16
CuE3N	11.11	3.88	0.16
CuE5N	18.97	8.17	0.16
CuE7N	32.74	14.26	0.16
ZCuE3N	4.04	2.01	<0.1
ZCuE5N	4.98	2.78	<0.1
ZCuE7N	5.83	2.41	<0.1

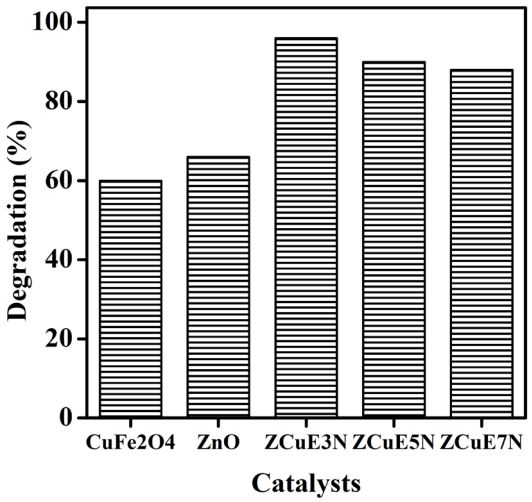

Figure 10. Graph of variations in catalyst types on Rhodamine B's degradation (treatment conditions: catalyst amount 20 mg, dye concentration 10 mg/L, dye volume 20 mL, and irradiation time 2 h).

The optimal concentration for Rhodamine B degradation by the composite was identified by varying the dye concentration (10-30 mg L^{-1}) with experimental conditions of the ZCuE3N catalyst amount of 20 mg, the irradiation time of 2 h, and the Rhodamine B solution volume of 20 mL. Figure 11a shows that the optimal concentration was reached at a Rhodamine B concentration of 10 mg L^{-1}. Higher dye concentrations in the liquid resulted in reduced degradation percentages; this is due to the increased number of dye molecules in the solution that prevents the penetration of light into the catalyst. As a result, the number of hydroxide radicals (OH·) produced from the photocatalytic process decreased. Additionally, hydroxide radicals are known to be the groups responsible for the photocatalytic process in solutions in the presence of light. Furthermore, increasing the concentration of the dye causes the formation of active sites in the catalyst to be reduced; thus, there is a decrease in the degradation of the dye[40,41].

As shown in Figure 11b, the effects of irradiation time on the percent degradation of the dye were analyzed by varying the exposure time (1-3 h) using ZCuE3N as a catalyst. The graph showed that the longer exposure time resulted in more amount of Rhodamine B dye will be degraded. This can be explained as follows; when the catalyst absorbs a certain amount of energy from the light, there is an excitation of electrons from the valence band (VB) to the conduction band (CB), which leaves a hole (h^+) in VB (Figure 12). The electrons in CB react with oxygen in the liquid to form O_2 and then react with H^+ from the dissociation of water molecules to form hydroxide radicals (OH·). Hydroxide radicals are responsible for the photodegradation of organic compounds in water. On the other hand, h^+ in CB reacts with OH^- from water to form OH·. Thus, in this photocatalytic process, a redox reaction takes place, where the oxidation process occurs in VB while the reduction process occurs in CB[24]. The general reaction mechanism was presented in the following relations;

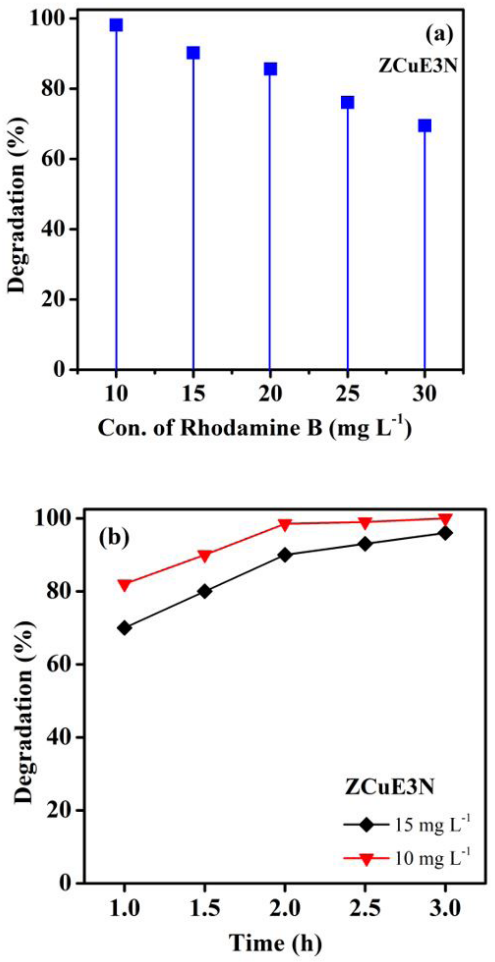

Figure 11. The effect of Rhodamine B concentration (a) and exposure time (b) on photocatalytic degradation using ZCuE3N as catalysts.

$$ZnO/CuFe_2O_4 + h\upsilon(Vis) \rightarrow ZnO/CuFe_2O_4\left(e^- CB + h^+ VB\right) \quad (3)$$

$$ZnO/CuFe_2O_4\left(e^- CB\right) + O_2 \rightarrow \bullet O_2^- \quad (4)$$

$$\bullet O_2^- + H^+ \leftrightarrow HOO\bullet \quad (5)$$

$$2HOO\bullet \rightarrow H_2O_2 + O_2 \quad (6)$$

$$H_2O_2 \rightarrow 2HO\bullet \quad (7)$$

$$ZnO/CuFe_2O_4\left(h^+ VB\right) + H_2O \rightarrow HO\bullet + H^+ \quad (8)$$

$$Dye + HO\bullet + \bullet O_2^- \rightarrow CO_2 + H_2O\ \left(By-product\right) \quad (9)$$

The catalyst efficiency test (reusability) evaluates the capacity of heterogeneous catalysts to be reused. This ability is very important to support its application in the industrial field. As a heterogeneous catalyst with magnetic properties, ZCuE3N can be easily separated from the solution using an external magnet and subjected to the next cycle as depicted

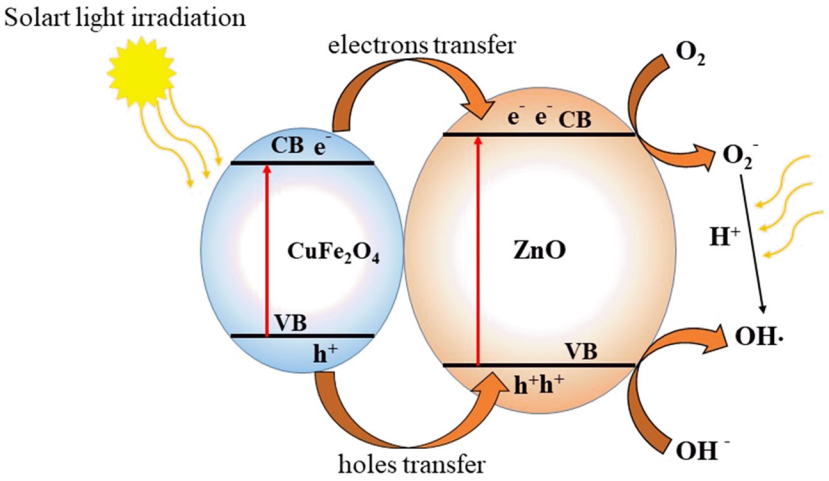

Figure 12. Schematic of the energy band structure and the process of separating the e^-- h^+ pairs of ZnO/$CuFe_2O_4$ composite.

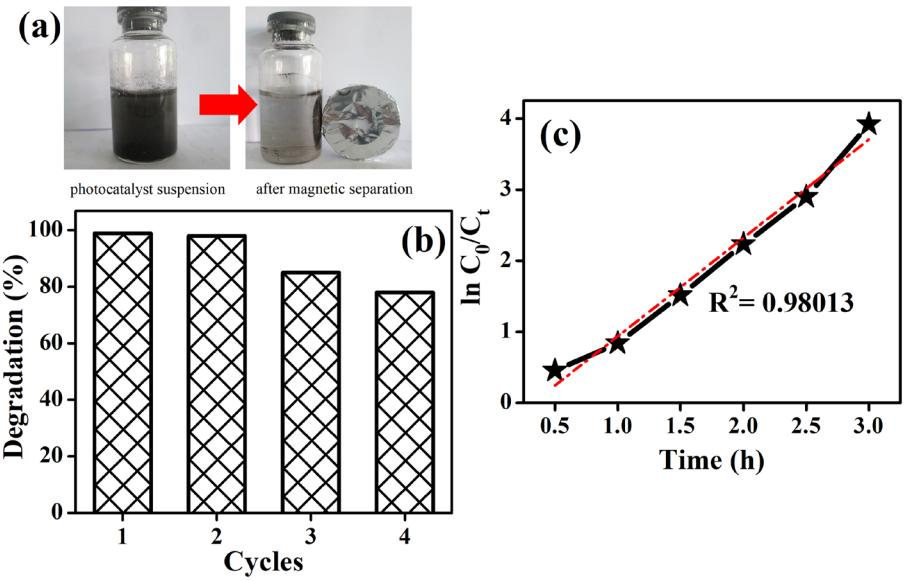

Figure 13. (a) Photographs of the ZCuE3N photocatalyst suspension before and after magnetic separation (b) reusability test and (c) kinetic curve of ZCuE3N catalyst for Rhodamine B.

in Figure 13a. The ZCuE3N powder was cleaned and dried to remove the particle dyes, hence give a more accurate degradation percentage in subsequence use. The catalyst efficiency test was carried out at a dye concentration of 10 mg L^{-1} and irradiation time of 2 h. From Figure 13b, it can be seen that the ability of the ZCuE3N catalyst is still good to continuously used, indicating the chemical stability of this composite. It is known that the metal oxide composite is stable and does not easily ionize in water. The reduced ability of the catalyst to degrade Rhodamine B after the third use may be due to the agglomeration of composite samples during the washing and drying process. This could reduce the specific surface area or the active site of the catalyst that reacts with the Rhodamine B dye.

Generally, kinetics for photocatalysis is described in the Langmuir-Hinshelwood model, which can be expressed by the following equation.

$$ln\left(C_0 / C_t\right) = k\,t \tag{10}$$

where C_0 is the initial concentration of Rhodamine B, C_t is the concentration at time t and k is the apparent first-order rate constant. By plotting $ln(C_0/C_t)$ vs irradiation time t can be determined the k, which can be used as an assessment index for evaluating the photocatalytic efficiency of synthesized materials[42]. From Figure 13c we can see that the kinetic plot for all catalysts is approximately linear. The k value for ZCuE3N nanoparticles is 1.224x10^{-2} mole L^{-1} min^{-1} in which indicates that ZCuE3N can be a good photocatalyst in and solar light.

4. Conclusion

In this work, ZnO/$CuFe_2O_4$ nanorod composites were synthesized by the hydrothermal method using rambutan peel extract as a natural capping agent. The XRD pattern and FT-IR results confirm the formation of the wurtzite structure of ZnO and the spinel structure of $CuFe_2O_4$ in composites. The morphology of the sample analyzed by SEM and TEM shows that the composite particles have a rod-like shape. EDX mapping confirms the distribution of elements in the composite. Furthermore, the band gaps estimated from optical studies confirmed that all the materials could act as photocatalysts under visible light with bandgap energy around 2.7 eV. The magnetic properties of the composites measured by VSM indicated that the ZnO/$CuFe_2O_4$ composites are superparamagnetic. The composites exhibited high photocatalyst activities for the degradation of Rhodamine B driven by solar light leading to complete degradation in 2 h. The use of magnetically separable ZnO/$CuFe_2O_4$ nanoparticles can be extended for the degradation of other harmful azo-dyes under sunlight.

5. Acknowledgments

The corresponding author would like to acknowledge the financial support by LPPM of Andalas University for this work through the KRPGB grant with contract number: SP DIPA 023.017.2.677513/2020.

6. References

1. Afkhami A, Moosavi R. Adsorptive removal of Congo red, a carcinogenic textile dye, from aqueous solutions by maghemite nanoparticles. J Hazard Mater. 2010;174(1–3):398-403.
2. Bayat M, Javanbakht V, Esmaili J. Synthesis of zeolite/nickel ferrite/sodium alginate bionanocomposite via a co-precipitation technique for efficient removal of water-soluble methylene blue dye. Int J Biol Macromol. 2018;116:607-19.
3. Jha M, Ansari S, Shimpi NG. Ultrasonic assisted green synthesis of Ag: CdO nanocubes and nanospheres using Citrus limon leaves for ef fi cient degradation of organic dyes. J Ind Eng Chem. 2019;69:269-84.
4. Somraksa W, Suwanboon S, Amornpitoksuk P, Randorn C. Physical and photocatalytic properties of CeO_2/ZnO/$ZnAl_2O_4$ ternary nanocomposite prepared by co-precipitation method. Mater Res. 2020;23(1):1-10.
5. Camacho-González MA, Quezada-Cruz M, Cerón-Montes GI, Ramírez-Ayala MF, Hernández-Cruz LE, Garrido-Hernández A. Synthesis and characterization of magnetic zinc-copper ferrites: antibacterial activity, photodegradation study and heavy metals removal evaluation. Mater Chem Phys. 2019;236:121808.
6. Adeleke JT, Theivasanthi T, Thiruppathi M, Swaminathan M, Akomolafe T, Alabi AB. Photocatalytic degradation of methylene blue by ZnO/$NiFe_2O_4$ nanoparticles. Appl Surf Sci. 2018;455:195-200.
7. Neelgund GM, Oki A. ZnO conjugated graphene: an efficient sunlight driven photocatalyst for degradation of organic dyes. Mater Res Bull. 2020;129:110911.
8. Pandiyarajan T, Karthikeyan B. Optical properties of annealing induced post growth ZnO:$ZnFe_2O_4$ nanocomposites. Spectrochim Acta A Mol Biomol Spectrosc. 2013;106:247-52.
9. Sun M, Han X, Chen S. Synthesis and photocatalytic activity of nano-cobalt ferrite catalyst for the photo-degradation various dyes under simulated sunlight irradiation. Mater Sci Semicond Process. 2019;91:367-76.
10. Gao J, Du Z, Ma S, Cheng F. High-efficiency leaching of valuable metals from saprolite laterite ore using pickling waste liquor for synthesis of spinel-type ferrites MFe_2O_4 with excellent magnetic properties. J Mater Res Technol. 2020;10:988-1001.
11. Lu C, Bao Z, Qin C, Dai L, Zhu A. Facile fabrication of heterostructured cubic-$CuFe_2O_4$/ZnO nanofibers (c-CFZs) with enhanced visible-light photocatalytic activity and magnetic separation. RSC Advances. 2016;6(111):110155-63.
12. Li Z, Lyu J, Ge M. Synthesis of magnetic Cu/$CuFe_2O_4$ nanocomposite as a highly efficient Fenton-like catalyst for methylene blue degradation. J Mater Sci. 2018;53(21):15081-95.
13. Ali K, Iqbal J, Jan T, Ahmad I, Wan D, Bahadur A, et al. Synthesis of $CuFe_2O_4$-ZnO nanocomposites with enhanced electromagnetic wave absorption properties. J Alloys Compd. 2017;705:559-65.
14. Karunakaran C, Vinayagamoorthy P, Jayabharathi J. $CuFe_2O_4$-encapsulated ZnO nanoplates: magnetically retrievable biocidal photocatalyst. J Nanosci Nanotechnol. 2017;17(7):4489-97.
15. Kumar A, Rout L, Achary LSK, Mohanty SK, Dash P. A combustion synthesis route for magnetically separable graphene oxide-$CuFe_2O_4$-ZnO nanocomposites with enhanced solar light-mediated photocatalytic activity. New J Chem. 2017;41(19):10568-83.
16. Paydar S, Akbar N, Shi Q, Wu Y. Developing cuprospinel $CuFe_2O_4$–ZnO semiconductor heterostructure as a proton conducting electrolyte for advanced fuel cells. Int J Hydrogen Energy. 2021;46:9927-37.
17. Yuvakkumar R, Suresh J, Nathanael AJ, Sundrarajan M, Hong SI. Rambutan (Nephelium lappaceum L.) peel extract assisted biomimetic synthesis of nickel oxide nanocrystals. Mater Lett. 2014;128:170-4.
18. Kotelnikova SV, Suslonov VV, Voznesenskiy MA, Bobrysheva NP, Osmolowsky MG, Rajabi F, et al. Effect of capping agents on Co polyol particles morphology, magnetic and catalytic properties. Mater Chem Phys. 2019;223:745-50.
19. Basnet P, Inakhunbi Chanu T, Samanta D, Chatterjee S. A review on bio-synthesized zinc oxide nanoparticles using plant extracts as reductants and stabilizing agents. J Photochem Photobiol B. 2018;183:201-21.
20. Rahmayeni AS, Jamarun N, Emriadi, Stiadi Y. Magnetically separable ZnO-$MnFe_2O_4$ nanocomposites synthesized in organic-free media for dye degradation under natural sunlight. Orient J Chem. 2017;33(6):2758-65
21. Manikandan A, Sridhar R, Antony SA, Ramakrishna S. A simple aloe vera plant-extracted microwave and conventional combustion synthesis : morphological, optical, magnetic and catalytic properties of $CoFe_2O_4$ nanostructures. J Mol Struct. 2014;1076:188-200.
22. Gingasu D, Mindru I, Patron L, Calderon-Moreno JM, Mocioiu C, Preda S, et al. Green synthesis methods of CoFe2O4 and Ag-CoFe2O4 nanoparticles using hibiscus extracts and their antimicrobial potential. J Nanomater. 2016;2016:2106756.
23. Rahmayeni PJ, Stiadi Y. Green synthesis of $NiFe_2O_4$ spinel ferrites magnetic in the presence of Hibiscus rosa-sinensis leaves extract: morphology, structure and activity. Rasayan J Chem. 2019;12(4):1942-9.
24. Rahmayeni AA, Stiadi Y, Lee HJ, Zulhadjri. Green synthesis and Characterization of ZnO-$CoFe_2O_4$ Semiconductor Photocatalysts Prepared Using Rambutan (Nephelium lappaceum L.) Peel Extract. Mater Res. 2019;22(5):2-11.
25. Priya M, Premkumar VK, Vasantharani P, Sivakumar G. Structural and electrochemical properties of $ZnCo_2O_4$ nanoparticles synthesized by hydrothermal method. Vacuum. 2019;167:307-12.
26. Cahyana AH, Liandi AR, Yulizar Y, Romdoni Y, Wendari TP. Green synthesis of $CuFe_2O_4$ nanoparticles mediated by Morus alba L. leaf extract: crystal structure, grain morphology, particle size, magnetic and catalytic properties in Mannich reaction. Ceram Int. 2021;47:21373-80.

27. Lutukurthi DNVVK, Dutta S, Behara DK. Effect of ignition temperature and fuel amount on photocatalytic activity of solution combustion synthesized ZnO. Ceram Int. 2020;46(14):22419-28.
28. Satheeshkumar MK, Kumar ER, Srinivas C, Prasad G, Meena SS, Pradeep I, et al. Structural and magnetic properties of $CuFe_2O_4$ ferrite nanoparticles synthesized by cow urine assisted combustion method. J Magn Magn Mater. 2019;484:120-5.
29. Amiri M, Salavati-Niasari M, Akbari A. Magnetic nanocarriers: evolution of spinel ferrites for medical applications. Adv Colloid Interface Sci. 2019;265:29-44.
30. Mahmoodi NM, Bashiri M, Moeen SJ. Synthesis of nickel-zinc ferrite magnetic nanoparticle and dye degradation using photocatalytic ozonation. Mater Res Bull. 2012;47(12):4403-8.
31. Sukriti CP, Singh V, Kumar D. Rapid visible light-driven photocatalytic degradation using Ce-doped ZnO nanocatalysts. Vacuum. 2020;178:109364.
32. Patil SB, Naik HSB, Nagaraju G, Viswanath R, Rashmi SK, Kumar MV. Sugarcane juice mediated eco-friendly synthesis of visible light active zinc ferrite nanoparticles: application to degradation of mixed dyes and antibacterial activities. Mater Chem Phys. 2018;212:351-62.
33. Soto-Arreola A, Huerta-Flores AM, Mora-Hernández JM, Torres-Martínez LM. Comparative study of the photocatalytic activity for hydrogen evolution of MFe_2O_4 (M = Cu, Ni) prepared by three different methods. J Photochem Photobiol Chem. 2018;357:20-9.
34. Karunakaran C, Vinayagamoorthy P, Jayabharathi J. Enhanced photocatalytic activity of magnetically separable bactericidal $CuFe_2O_4$-embedded Ag-deposited ZnO nanosheets. RSC Advances. 2016;6(3):1782-91.
35. Gingasu D, Mindru I, Mocioiu OC, Preda S, Stanica N, Patron L, et al. Synthesis of nanocrystalline cobalt ferrite through soft chemistry methods: a green chemistry approach using sesame seed extract. Mater Chem Phys. 2016;182:219-30.
36. Anandan S, Selvamani T, Prasad GGM, Asiri AJ, Wu J. Magnetic and catalytic properties of inverse spinel $CuFe_2O_4$ nanoparticles. J Magn Magn Mater. 2017;432:437-43.
37. Bayat R, Derakhshi P, Rahimi R, Safekordi AA, Rabbani M. A magnetic $ZnFe_2O_4$ /ZnO/perlite nanocomposite for photocatalytic degradation of organic pollutants under LED visible light irradiation. Solid State Sci. 2019;89:167-71.
38. Xu Y, Li W, Zuo X, Li Y, Zhang C, Min N, et al. Nanoprecipitation-suppressed ferrite transformation ($\gamma \rightarrow \alpha$) during tempering in a mediummanganese steel. Scr Mater. 2019;162:391-6.
39. Dhiman M, Chudasama B, Kumar V, Tikoo KB, Singhal S. Augmenting the photocatalytic performance of cobalt ferrite via change in structural and optical properties with the introduction of different rare earth metal ions. Ceram Int. 2019;45(3):3698-709.
40. Arimi A, Megatif L, Granone LI, Dillert R, Bahnemann DW. Visible-light photocatalytic activity of zinc ferrites. J Photochem Photobiol Chem. 2018;366:118-26.
41. Arunadevi R, Kavitha B, Rajarajan M, Suganthi A. Sonochemical synthesis and high-efficient solar-light-driven photocatalytic activity of novel cobalt and manganese codoped tungsten oxide nanoparticles. Chem Phys Lett. 2019;715:252-62.
42. Aghabeikzadeh-Naeini E, Movahedi M, Rasouli N, Sadeghi Z. Synthesis of $ZnFe_2O_4$ nanoparticles in presence and absence of Tween-20: optical property, adsorption and photocatalytic activity. Mater Sci Semicond Process. 2018;73:72-7.